Journal of Applied Physics

RESEARCH ARTICLE | MARCH 27 2024

Investigating the effects of sum-frequency conversions and surface impedance uniformity in traveling wave superconducting parametric amplifiers

Nikita Klimovich ; Samuel Wood ; Peter K. Day ; Boon-Kok Tan

J. Appl. Phys. 135, 124402 (2024)
https://doi.org/10.1063/5.0192030

AIP Publishing

Journal of Applied Physics ARTICLE pubs.aip.org/aip/jap

Investigating the effects of sum-frequency conversions and surface impedance uniformity in traveling wave superconducting parametric amplifiers

Cite as: J. Appl. Phys. **135**, 124402 (2024); doi: 10.1063/5.0192030
Submitted: 18 December 2023 · Accepted: 7 March 2024 ·
Published Online: 27 March 2024

Nikita Klimovich,[1,a)] Samuel Wood,[2] Peter K. Day,[3] and Boon-Kok Tan[1]

AFFILIATIONS

[1]Department of Physics (Astrophysics), University of Oxford, Denys Wilkinson Building, Keble Road, Oxford OX1 3RH, United Kingdom
[2]The Queen's College, University of Oxford, High Street, Oxford OX1 4AW, United Kingdom
[3]Jet Propulsion Laboratory, California Institute of Technology, Pasadena, California 91109, USA

[a)]**Author to whom correspondence should be addressed:** nikita.klimovich@physics.ox.ac.uk

ABSTRACT

Traveling wave parametric amplifiers (TWPAs) offer the most promising solution for high gain, broadband, and quantum noise limited amplification at microwave frequencies. Experimental realization of TWPAs has proved challenging with often major discrepancies between the theoretically predicted and the measured gain performance of the devices. Here, we extend the conventional modeling techniques to account for spatial variation in the surface impedance of the thin film and the parametric sum-frequency conversions effect, which subsequently results in accurate reproduction of experimental device behavior. We further show that such an analysis may be critical to ensure fabricated TWPAs can operate as designed.

I. INTRODUCTION

The growing number of sensitive experiments within the fields of quantum computing, dark matter searches, and astronomical detectors have generated a growing need for broadband low-noise amplifiers at microwave frequencies. Traveling wave parametric amplifiers (TWPAs) have risen to meet this need thanks to their potential to reach the noise performance at the theoretical standard quantum limit.[1] Although narrow band devices based on Josephson junctions are already a fairly mature technology,[2] the demonstration of the first working TWPA based on the kinetic inductance of a superconducting transmission line in 2012[3] generated immense interest due to the simpler design, higher power handling capability, and ease of fabrication.

In recent years, kinetic inductance (KI)TWPAs have demonstrated excellent gain and noise performance, but the technology has yet to become widely available.[4,5] While many publications focus on theoretical developments, modeling techniques, and proposals for new designs, only a few have reported successful experimental demonstrations of functional devices.[6–11] The predicted gain performance is often not included for comparison with these experimental results, potentially due to discrepancies between the theoretical models and the measured responses, as well as fabrication inconsistencies.

In this paper, we expand upon the commonly used theoretical model for designing and predicting TWPA performance, by incorporating the often-neglected sum-frequency processes that occur within the TWPA, and the impact of surface impedance inhomogeneity in the long TWPA lines. These additions allow us to more accurately represent the measured performance of our niobium titanium nitride (NbTiN) TWPA device operating in the three-wave mixing (3WM) regime. We demonstrate that with this extended model, we can achieve excellent agreement between the

predicted gain profile and the measured results, including the sum-frequency profiles. We argue that incorporating the effect of sum-frequency generation in the design process is crucial to ensure that the fabricated TWPAs behave as intended.

II. GENERALIZED COUPLED MODE EQUATIONS

Using the slow-varying amplitude and undepleted pump approximations, the standard coupled mode equations for 3WM gain ($\Delta k_g = k_s + k_i - k_p$, where k_s, k_i, and k_p are the wavenumbers of the signal, idler, and pump) are given by[12]

$$\frac{\partial A_p}{\partial z} = \frac{ik_p}{8I_*^2}\left[A_p^2 A_p^* + 4I_{dc}^2 A_p\right],$$
$$\frac{\partial A_s}{\partial z} = \frac{ik_s}{8I_*^2}\left[\left(2|A_p|^2 + 4I_{dc}^2\right)A_s + 4I_{dc}A_p A_i^* e^{-i\Delta k_g z}\right], \quad (1)$$
$$\frac{\partial A_i}{\partial z} = \frac{ik_i}{8I_*^2}\left[\left(2|A_p|^2 + 4I_{dc}^2\right)A_i + 4I_{dc}A_p A_s^* e^{-i\Delta k_g z}\right],$$

in the limit where the pump amplitude and DC-biased current are much stronger than the signal and idler amplitudes (A_p, $I_{dc} \gg A_s$, A_i), hence removing terms with more than one A_s or A_i to further simplify the expression. These simplified expressions and their analytic solutions have been used to design and simulate numerous TWPAs,[3,8] but a more nuanced approach may sometimes be necessary.

Most of the assumptions taken in formulating the above expressions are adequate to predict the performance of a typical TWPA, although accounting for transmission line losses can yield a slightly better match with measured results. Nevertheless, most models struggle to produce a simulated curve that agrees well with the measured profile. We believe that this is because these coupled mode equations (CMEs) models do not take into account the effect of pump harmonics generation and various sum-frequency up-conversion processes such as $p+s$, $p+i$, $2p+s$, $2p+i$ (in the 3WM mode), etc. Each of these processes not only alters the above expressions but also adds an additional pair of equations to be considered. As an example, the first-order 3WM sum-frequency generation of $p+s$ and $p+i$ adds the following equations to the CMEs:

$$\frac{\partial A_{p+s}}{\partial z} = \frac{ik_{p+s}}{8I_*^2}\left[\left(2|A_p|^2 + 4I_{dc}^2\right)A_{p+s} + 4I_{dc}A_p A_s e^{-i\Delta k_{u,s} z}\right], \quad (2)$$

$$\frac{\partial A_{p+i}}{\partial z} = \frac{ik_{p+i}}{8I_*^2}\left[\left(2|A_p|^2 + 4I_{dc}^2\right)A_{p+i} + 4I_{dc}A_p A_i e^{-i\Delta k_{u,i} z}\right], \quad (3)$$

(where $\Delta k_{u,n} = k_{p+n} - k_p - k_n$) as well as the following additional terms to Eq. (1)

$$\frac{\partial A_s}{\partial z} = \left(\cdots\right) + \frac{ik_s}{8I_*^2}\left[4I_{dc}A_p^* A_{p+s} e^{-i\Delta k_{i'} z}\right], \quad (4)$$

$$\frac{\partial A_i}{\partial z} = \left(\cdots\right) + \frac{ik_i}{8I_*^2}\left[4I_{dc}A_p^* A_{p+i} e^{-i\Delta k_{i'} z}\right], \quad (5)$$

where $\Delta k_{n'} = k_n + k_p - k_{p+n}$. Depending on the dispersion relation of the TWPAs, these additional terms can significantly affect the profile of the sought-after primary 3WM gain. A thorough modeling including these parameters is thus required to determine the robustness of any design against these parametric sum-frequency terms.

Because of the large number of possibly relevant harmonic generation or frequency conversion processes in a TWPA, we include all possible first- and second-order parametric terms in our analysis. We define the first-order terms as any combination of pump, signal, and idler frequencies (containing at least one pump for 3WM or two pumps for 4WM) and second-order terms similarly but containing any combination of the pump second or third harmonic instead. The large number of required CMEs are generated through numerical expressions detailed in Appendix A, which amount to a systematic search of every energetically allowed combination of frequencies.

III. DEVICE DESIGN

The general design principles of our NbTiN devices have been reported in detail previously,[12] hence only a short description of the device is provided here for completeness. Our device uses a thin NbTiN superconducting film deposited on a silicon substrate with an amorphous silicon (aSi) dielectric and NbTiN ground plane on top to form an inverted microstrip structure. The inverted microstrip geometry is shown to protect the conduction layer beneath the less sensitive ground plane. The device geometry and critical material parameters are given in Table I. The central conductor is 96.69 mm in physical length and is meandered back and forth 50× with a minimum bending radius of 250 μm to fit within the 2.5 cm by 0.7 cm physical footprint.[5]

A diagram of a unit cell is shown in Fig. 1. The central conductors are extended every $d = 2\,\mu$m with stubs (same width as the central strip) to provide additional capacitance to the ground while having only a minimal effect on the inductance of the central line. These capacitive stubs serve three primary purposes: (1) introducing additional capacitance to counteract the high inductance for $\sqrt{L/C} = 50\,\Omega$ impedance matching, (2) acting as quarter-wave resonators near 100 GHz for generating stronger dispersion at high frequencies, and (3) sinusoidal modulation in their length to introduce a stopband near 9 GHz used for phase matching the 3WM process.

TABLE I. Design parameters of the parametric amplifier, including material properties of the NbTiN conductor and ground (normal state resistivity ρ, and critical temperature T_c); central conductor, dielectric, and ground plane thicknesses (t_{ms}, t_ϵ, t_{gnd}); central conductor width (w); and capacitive stub spacing (d), average length (l_0), modulation amplitude and period (l_a, λ_p).

NbTiN parameters		Film thickness			Central conductor geometry				
ρ	T_c	t_{ms}	t_ϵ	t_{gnd}	w	d	l_0	l_a	λ_p
260 $\mu\Omega$cm	14.5 K	35 nm	190 nm	200 nm	250 nm	2 μm	26 μm	4 μm	110 μm

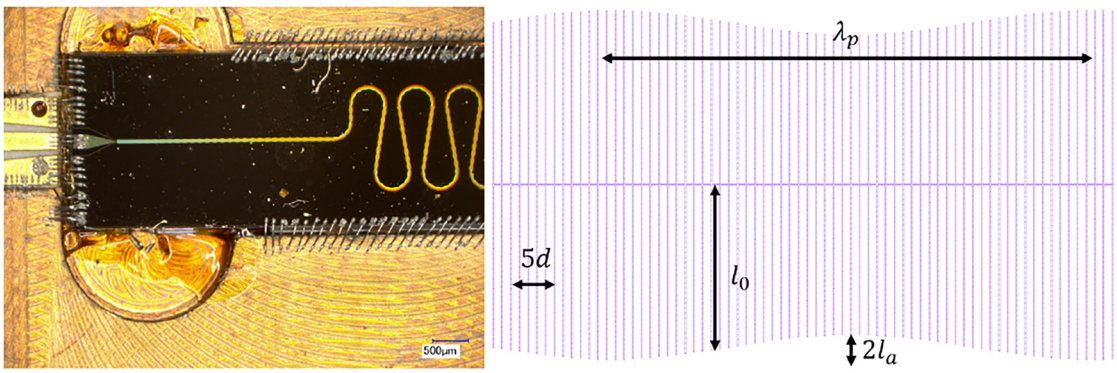

FIG. 1. (Left) A photo of the device showing the bond pad, transmission line, and several of the meanders. (Right) A visual depiction of the transmission line structure consisting of a capacitive stubs of length $L = l_0 + l_a \sin(2\pi dz/\lambda_p)$ and transmission line sections of length d.

The second point is particularly critical for the working of this device. The nonlinear component of the dispersion curve, shown in Fig. 2, remains relatively small at frequencies below 10 GHz but rapidly increases thereafter. This nonlinearity mismatches the dispersion criteria for the production of any higher frequency processes including sum-frequency generation and pump harmonics, limiting the latter to less than 1% of the incident pump power. Because these undesirable parametric processes are poorly phase-matched rather than fully suppressed, they are still relevant and are experimentally explored in the following section.

IV. RESULTS

The behavior of the device was measured at 10 mK in a simple cryogenic setup consisting of unattenuated coaxial lines with a pair of bias tees and switches surrounding the device at the mixing chamber stage. The device's transmission profile is presented in Fig. 3, showing a relatively clean transmission with the stopband clearly visible near the designed 9 GHz, plotted in red. One note immediately, however, is that the measured width of the stopband (blue) is substantially wider than the prediction (red).

Given that the dimensions of the transmission line are relatively insensitive to fabrication defects (especially with the e-beam fabrication technique utilized for our device) and can be verified with a high-magnification microscope, we do not expect this discrepancy results from dimensional fabrication error. We also do not expect the film thicknesses or dielectric constants of materials used to deviate significantly from the designed values during fabrication within our controlled environment. However, the resistivity of thin superconducting film deposited through sputtering is very sensitive to the fabrication conditions and can vary by as much as a factor of 2 across a wafer.[13]

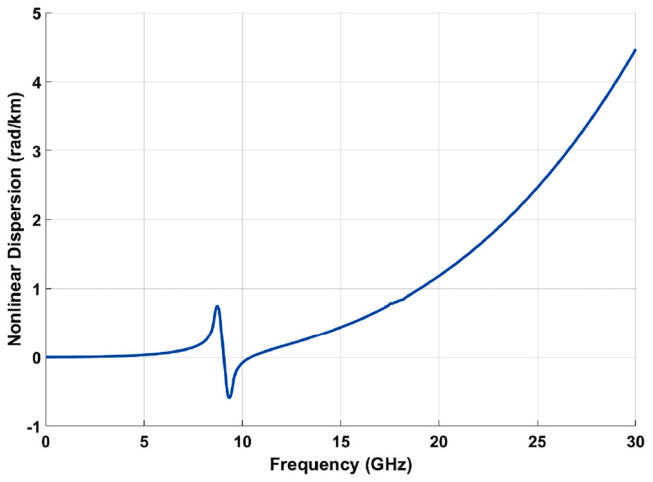

FIG. 2. The nonlinear component of the dispersion, defined as $k - 2\pi\omega/v_{ph}$ where v_{ph} is computed in the low-frequency limit.

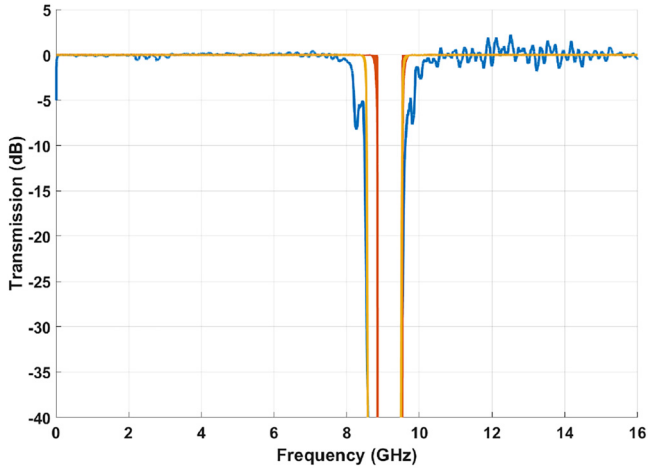

FIG. 3. Experimentally measured transmission (blue), theoretical transmission with $\rho = 259\,\mu\Omega$ cm (red), and theoretical transmission with $\rho = 259$–$281\,\mu\Omega$ cm (yellow).

To recover the true behavior of the device that matches the measured transmission profile, we therefore re-simulate our TWPA using all the parameters tabulated in Table I as designated, except for the normal state resistivity ρ (note that the effects of ρ in our model are degenerate with T_c, so any combination of tuning those parameters can result in the same effect). Assuming the resistivity of the NbTiN film across the wafer may not be constant at exactly the desired 260 $\mu\Omega$cm results in a variation in surface inductance at different parts of the transmission line, and hence the stopband frequencies along the transmission line.

The overall stopband seen in the S_{21} will be a combination of the individual varying stopbands formed by each segment along the line. The minimum and maximum frequency extent of the overall stopband in the S_{21} thus determine the extrema resistivity values seen along the line. Fitting the edges of the gap as shown in Fig. 3, we find that our resistivity must vary from 259 to 281 $\mu\Omega$ cm along the line. If we assume the variation is linear between these two values, we successfully reproduce and match the position and the width of the measured stopband with only a small deviation near the edges. The regions very near the gap are greatly affected by its internal structure, so applications with pumps operating very near the gap may require additional analysis to model the exact resistivity profile.

Having performed the surface impedance recovery, we proceed to investigate the correspondence between the experimentally measured and theoretically predicted gain performance of the device. A measured pump-on/off gain curve is shown in Fig. 4 alongside the theoretical calculations with and without the sum-frequency contribution. As can be seen from the figure, the model containing the first order $p+s$ and $p+i$ sum-frequency terms (red) is almost indistinguishable from the smoothed experimental data. Note that to reproduce this gain curve, the only parameter we slightly adjusted was the pump power to take into account the experimental uncertainties of the transmission within our setup.

On the other hand, taking into consideration exactly identical operating conditions but a model without surface impedance recovery or sum frequency terms considered results in the poorly matched yellow curve in Fig. 4. The shift in the stopband due to the variation in film resistivity slightly alters the frequency at which optimal phase matching occurs. Since the pump frequency was tuned to provide the best experimentally realized gain, we see a lower gain in the simulation. Even if the same dispersion is considered in both cases to correct for the average level of gain, the shape of the gain profile in the experiment remains flatter and broader than the simple coupled mode prediction without the inclusion of the sum-frequency terms. Only by taking both effects into account can the model reproduce the measured data.

To further validate our extended model, we used the mixer mode of our vector network analyser (VNA) to measure the $p+s$ and $p+i$ components, as shown in Figs. 5 and 6, respectively. The x axis of these plots shows the input signal frequency with the y axis showing the relative power at the output $p+s$ and $p+i$ frequency with reference to the power of the signal at the input of the device. This is achieved by estimating the signal power at the device according to the S_{21} of our input lines and back-propagating the measured output power to the input of the device by subtracting the S_{21} of the output lines at the up-converted frequency. The output signal propagates at a significantly higher frequency than the input and thus experiences a cutoff from our room-temperature amplifier and SMA connectors near 18 GHz, corresponding to signal frequencies above 7 GHz for the $p+s$ measurement and signal frequencies below 4 GHz for the $p+i=p+(p-s)=2p-s$.

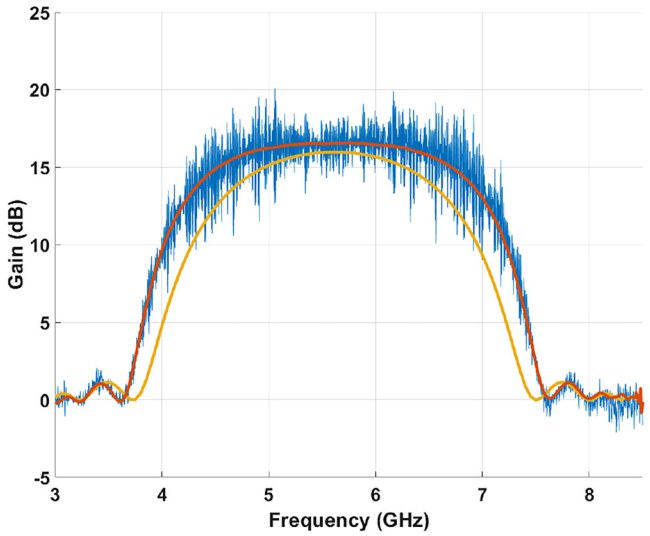

FIG. 4. Experimentally measured 3WM gain (blue) with the device pumped at 11.232 GHz, and the theoretical calculations shown with (red) and without (yellow) sum-frequency terms or resistivity variation considered.

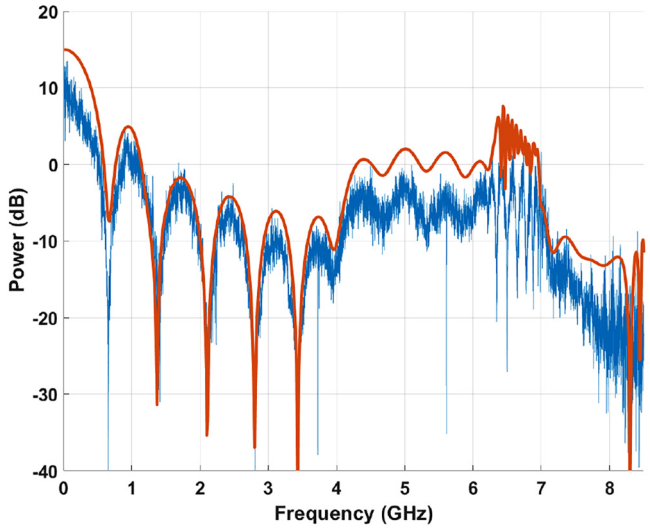

FIG. 5. Experimentally measured $p+s$ power (blue) calibrated to the output of the device relative to the signal power at the input, with theoretical calculation shown in red.

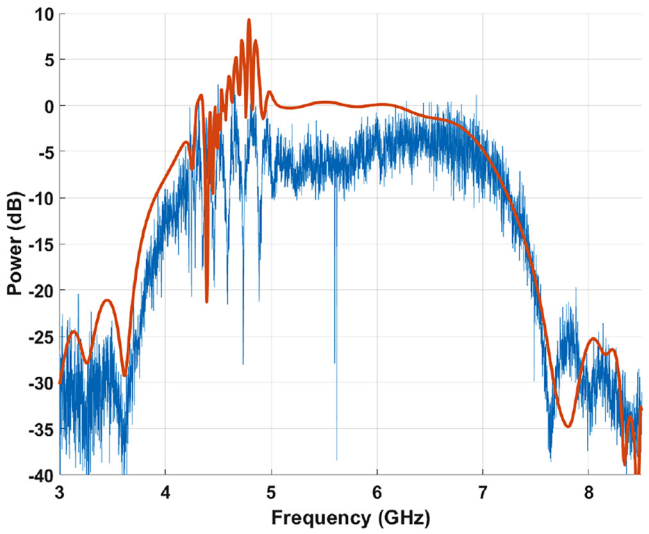

FIG. 6. Experimentally measured $p + i$ power (blue) calibrated to the output of the device relative to the signal power at the input, with theoretical calculation shown in red.

We again see excellent correspondence between the measured data and theoretical predictions, particularly in terms of matching the spectral features. Properly calibrating the S_{21} for a signal input at one frequency and output at another in the VNA's mixer mode is challenging and is likely responsible for much of the small amount of amplitude discrepancy shown. The periodic oscillation in $p + s$ power shown in Fig. 5 results from the phase mismatch for the conversion process, which causes signal power to be sinusoidally transferred back and forth between the up-conversion mode along the length of the line. The total output of the $p + s$ mode with respect to frequency thus also oscillates depending on whether the end of the TWPA corresponds to a peak or trough of the conversion process.

As the sinusoidal variation in resistivity is not continuous but only defined at each capacitive stub, a secondary, much smaller feature in the dispersion is produced at approximately twice the gap frequency (as can be seen near 17–18 GHz in Fig. 2). The rapid fluctuation in Fig. 5 between 6–7 GHz as well as between 4 and 5 GHz in Fig. 6 are the results of strong interactions between the sum-frequency tone with this second harmonic of the gap and are thus quite sensitive to its internal structure. In principle, these secondary effects could, therefore, be used to further refine the recovery of the exact spatial variation in film resistivity across the device.

V. DISCUSSION

We have obtained a nearly perfect reconstruction of the experimentally measured 3WM gain in our TWPA through a combination of detailed modeling techniques including secondary parametric effects and inhomogeneity of surface impedance. Accounting for superconducting film variation across the device is important not only for recovering the measured gain profile but also has several implications for device design. As shown in Fig. 7, small changes in resistivity across the device can result in major deviations from desired dispersion near the gap, and may significantly suppress gain for designs aiming to operate with a pump very near the gap. Variations in film parameters can be quite large, particularly near the edges of a wafer, but can also be stable and consistent.[13] In such cases, one could correct this effect in the device design, once the variation profile is known, and thereby increase the number of potentially working TWPAs from any given fabrication run.

The particular device design used here is fairly insensitive to these variations. In our device, the stopband at 9 GHz is much stronger than necessary to obtain optimal 3WM phase matching, meaning we must operate the pump at a frequency nearly 2 GHz higher than the gap to compensate. While this does somewhat lower the bandwidth of our device, an alternate design which intends to operate the pump too near the gap (e.g., at 8.5 GHz in Fig. 7) might not have any well phase-matched frequency to achieve similar broadband gain, given the 8% resistivity variations seen in our fabrication. As dispersion near the gap is so sensitive to its internal structure, a more detailed characterization or fit may be required than the linear approximation used in this work.

We have shown that the inclusion of other parametric processes, namely, 3WM conversion to and from the $p + s$ and $p + i$ modes, was crucial to properly reconstruct the experimentally measured data. Higher-order parametric processes were also included in our subsequent analysis, namely, the formation of the second and third pump harmonics as well as the conversion of the signal and idler from any of the resulting pump tones. However, due to the strong nonlinear dispersion of our device introduced via the capacitive stubs, the inclusion of any of these higher-frequency terms beyond $p + s$ and $p + i$ has no visible impact on the final result.

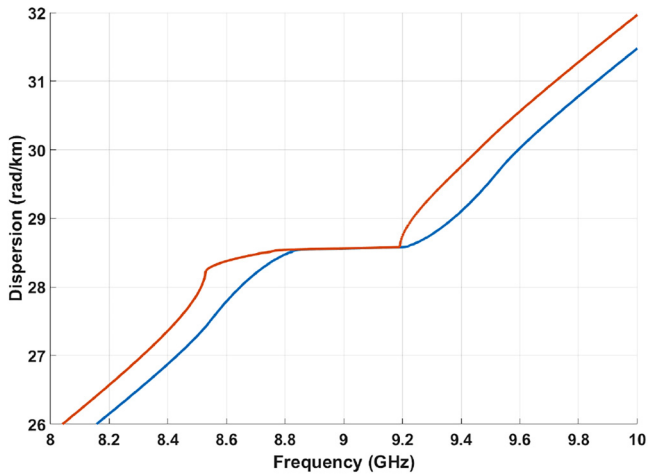

FIG. 7. Dispersion (wavenumber, k, as a function of frequency) introduced by the periodic stopband with ρ linearly (blue) and nonlinearly (red) varied ρ between 259 and 281 $\mu\Omega$ cm.

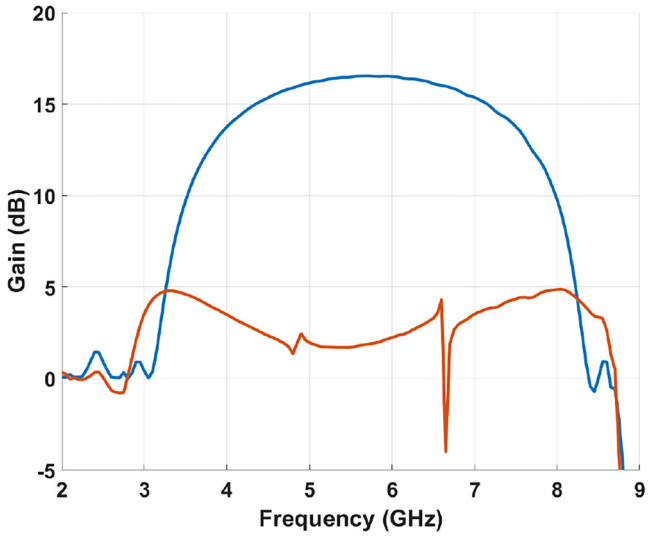

FIG. 8. Theoretical 3WM gain for a device identical to ours but without added dispersion, plotted in blue using the standard coupled mode equations and in red when considering other parametric processes.

Although the discrepancy between our enhanced model and the simplistic traditional CME techniques may seem relatively minor for this particular device, this is a product of numerous careful considerations undertaken during the design phase of our device, and may not hold true more generally. For example, a common approach taken by many is to minimize the dispersion introduced by the capacitive stubs to maximize the gain-bandwidth product. To demonstrate the difference between the two approaches, we alter our design by shortening the stub length but packing them closer to achieve the same capacitance per length as the original design. As shown in Fig. 8, one would expect an almost identical gain profile shown earlier, if we were to use the simplified CMEs model. However, it is clear from the plot that once the higher-frequency parametric conversion processes are taken into account, the gain profile nearly collapses to a negligible level. Depending on the particular design, the exact nature of this effect can be highly variable, resulting in an overall gain reduction, asymmetric amplification, or narrow-band dips within the gain profile. We suspect that this could be the reason that many published design papers struggle to reproduce the measured gain curve, or worse, fail to produce a working TWPA device, hence highlighting the importance of incorporating these secondary parametric conversion effects in the design phase.

VI. CONCLUSION

We have extended the commonly used modeling technique in the form of CMEs to include two practical considerations, i.e., the uniformity of surface impedance across the film and the effect of sum-frequency generation. We showed that by including these effects, we can successfully reproduce a gain profile that matched extremely well with experimentally measured results, hence validating our model. One important application of this technique is that we can recover the surface impedance of the actual devices populated across the wafer post-fabrication to better inform the next design phase. Furthermore, we showed that accounting for higher-order parametric processes is crucial for reproducing a measured gain profile; but more importantly, allowing for a well-considered TWPA design that has a higher chance of producing a working device, which we suspect that the combination of these effects is likely responsible for some of the difficulties encountered by many groups in translating their TWPA designs to the laboratory demonstration.

ACKNOWLEDGMENTS

The authors would like to acknowledge the European Research Council (ERC) program under Project No. 803862 (SPA4AstroQIT) for supporting this work. For the purpose of Open Access, the author has applied a CC BY public copyright licence to any Author Accepted Manuscript version arising from this submission.

AUTHOR DECLARATIONS

Conflict of Interest

The authors have no conflicts to disclose.

Author Contributions

Nikita Klimovich: Conceptualization (lead); Data curation (supporting); Investigation (lead); Methodology (lead); Software (lead); Validation (lead); Visualization (lead); Writing – original draft (lead); Writing – review & editing (supporting). **Samuel Wood:** Data curation (lead); Investigation (supporting); Methodology (supporting); Validation (supporting); Writing – review & editing (supporting). **Peter K. Day:** Formal analysis (supporting); Methodology (supporting); Resources (supporting); Software (supporting); Supervision (supporting); Validation (supporting); Writing – review & editing (supporting). **Boon-Kok Tan:** Conceptualization (supporting); Formal analysis (supporting); Funding acquisition (lead); Investigation (supporting); Methodology (supporting); Project administration (lead); Resources (lead); Supervision (lead); Writing – review & editing (lead).

DATA AVAILABILITY

The data that support the findings of this study are available from the corresponding author upon reasonable request.

APPENDIX A: GENERALIZED COUPLED MODE EQUATIONS

The coupled mode equations governing any set of frequencies ω_n with amplitudes A_n can be obtained from a combination of all possible 3WM and 4WM processes,

$$\frac{\partial A_n}{\partial z} = \text{3WM} + \text{4WM}, \tag{A1}$$

where the 3WM processes are given by[11]

$$\mathrm{3WM} = \frac{ik_n I_{dc}}{4I_*^2} \sum_{p,q\in\mathbb{N}_0} \sum_{\sum_j p_j + \sum_j q_j = 2} \frac{e^{ik_n z}}{p_1!\cdots p_m! q_1!\cdots q_m!} \times \delta\left(\sum_j p_j\omega_j - \sum_j q_j\omega_j - \omega_n\right) \times \prod_{1\le j\le N} \left(A_j e^{-ik_n z}\right)^{p_j} \prod_{1\le j\le N} \left(A_j^* e^{ik_n z}\right)^{q_j}, \tag{A2}$$

and the 4WM terms from

$$\mathrm{4WM} = \frac{ik_n}{4I_*^2} \sum_{p,q\in\mathbb{N}_0} \sum_{\sum_j p_j + \sum_j q_j = 3} \frac{e^{ik_n z}}{p_1!\cdots p_m! q_1!\cdots q_m!} \times \delta\left(\sum_j p_j\omega_j - \sum_j q_j\omega_j - \omega_n\right) \times \prod_{1\le j\le N} \left(A_j e^{-ik_n z}\right)^{p_j} \prod_{1\le j\le N} \left(A_j^* e^{ik_n z}\right)^{q_j}. \tag{A3}$$

These summations consider all combinations of emitted (p) and absorbed (q) photons that result in an emitted photon at frequency ω_n.

In the process of numerically solving the resulting coupled mode equations, we allow the device dispersion defined by k to itself vary as a function of position. This allows us to accurately simulate the effects of any tapered sections at the ends of the device as well as material variations throughout.

APPENDIX B: TRANSMISSION LINE MODELING

The dispersion of the resulting design is simulated using a modified version of a standard numerical model for inverted microstrips. We begin by taking the Bardeen–Cooper–Schrieffer (BCS)-theory approximation of $\Delta = 1.76 k_B T_c$ for the energy gap within our superconducting material based on the experimentally measured critical temperature T_c. The magnetic penetration depth λ is calculated using[14]

$$\lambda = 1/\sqrt{\mu_0 \omega \sigma_2}, \tag{B1}$$

where σ_2 is the imaginary part of the complex conductivity $\sigma = \sigma_1 - i\sigma_2$ and can be calculated from the Mattis–Bardeen theory[15] by evaluating

$$\frac{\sigma_2}{\sigma_N} = \frac{1}{\hbar\omega}\int_{\Delta-\hbar\omega}^{\Delta} \left(1 - \frac{2}{e^{(E+\hbar\omega)/kT}+1}\right) \frac{E^2+\Delta^2+E\hbar_\omega}{\sqrt{\Delta^2-E^2}\sqrt{(E+\hbar\omega)^2-\Delta^2}} dE, \tag{B2}$$

where σ_N is the bulk normal state resistivity and is determined by the deposition parameters used to grow the NbTiN film.

The basic geometry of our superconducting film (thickness t_s and width w), dielectric (thickness t_ϵ and dielectric constant ϵ_r), and ground plane (thickness t_g) is then used to compute the characteristic impedance Z_0 and ϵ_{eff} of our inverted microstrip using the methodology of Hammerstad and Jensen.[16] The inductance given by this computation according to $\mathcal{L}_0 = Z_0/v_{\mathrm{ph}}$ and $v_{\mathrm{ph}} = c/\sqrt{\epsilon_{\mathrm{eff}}}$ is adjusted for the surface inductance of both the conductor and ground according to

$$\mathcal{L} = \mathcal{L}_0 + \frac{\mathcal{L}_{\mathrm{surf,\,cond}}}{w} + \frac{\mathcal{L}_{\mathrm{surf,\,ground}}}{w_{\mathrm{eff}}}, \tag{B3}$$

where surface inductance is given by

$$\mathcal{L}_{\mathrm{surf}} = \mu_0 \lambda \coth t/\lambda, \tag{B4}$$

and the width of the current flow in the ground plane is set by the maximum of the conductor width, thickness, or Pearl length: $w_{\mathrm{eff}} = \max\left[w,\ \lambda_g^2,\ t_g\right]$. This value is then used to recompute an accurate prediction of the phase velocity, $v_{\mathrm{ph}} = 1/\sqrt{\mathcal{L}\mathcal{C}}$ and characteristic impedance of the line $Z = \sqrt{\mathcal{L}/\mathcal{C}}$. The phase velocity can be further adjusted for various operating conditions according to

$$v_{\mathrm{ph}}(I) = \frac{v_{\mathrm{ph}}(0)}{\sqrt{1+(I/I_*)^2}}, \tag{B5}$$

where I_* is an experimentally measured parameter.[11]

With the inductance, capacitance, and phase velocity of the microstrip geometry at hand, we compute the ABCD matrix of the transmission line by cascading the comprising unit cells. Each unit cell consists of the central microstrip section with length $d/2$ leading to the edge of each stub, the stub itself, and the remaining $d/2$ of the central microstrip to the start of the subsequent cell (see Fig. 1). Defining

$$\beta = \frac{2\pi\omega}{v_{\mathrm{ph}}}, \tag{B6}$$

the ABCD matrix for the transmission of a signal for the central transmission line (TRL) portion of the unit cell is[17]

$$\hat{A}_{\mathrm{TRL}} = \begin{bmatrix} \cos\left(\frac{d}{2}\beta\right) & iZ\sin\left(\frac{d}{2}\beta\right) \\ \frac{i}{Z}\sin\left(\frac{d}{2}\beta\right) & \cos\left(\frac{d}{2}\beta\right) \end{bmatrix}, \tag{B7}$$

and the ABCD matrix of the capacitive stubs is[17]

$$\hat{A}_{\mathrm{FIN}} = \begin{bmatrix} 1 & 0 \\ \frac{2i}{Z}\tan\left(L\beta\right) & 1, \end{bmatrix} \tag{B8}$$

where L is the length of the stub and the factor of 2 results from having two capacitive stubs. Finally, the combined ABCD matrix for each cell is simply the cascade of these elements,

$$\hat{A}_{\mathrm{CELL}} = \hat{A}_{\mathrm{TRL}}\hat{A}_{\mathrm{FIN}}\hat{A}_{\mathrm{TRL}}. \tag{B9}$$

The ABCD matrix for the amplifier as a whole is similarly the product of the ABCD matrices of each of the N cells comprising

the device

$$\hat{A} = \hat{A}_{\mathrm{CELL}}(1)\hat{A}_{\mathrm{CELL}}(2)\cdots\hat{A}_{\mathrm{CELL}}(N-1)\hat{A}_{\mathrm{CELL}}(N), \tag{B10}$$

where $\hat{A}_{\mathrm{CELL}}(n)$ denotes the ABCD matrix corresponding to the nth unit cell in the device. Each cell is calculated sequentially using the appropriate parameters given the position along the line to account for the periodic modulation of capacitive stub length, tapered amplitude of that modulation near the start and end of the line, and any material parameter variation across the device due to fabrication non-uniformity. We then calculate the S_{21} from the ABCD matrix and store it for use within the gain calculation. The resulting S_{21} from this calculation is saved at each step along the line and is used to calculate the spatially varying dispersion according to $k(z) = \mathrm{unwrap}(\mathrm{angle}(S_{21}(z)))$ used for gain calculation.

REFERENCES

[1]C. M. Caves, Phys. Rev. D **26**, 1817 (1982).
[2]M. A. Castellanos-Beltran and K. W. Lehnert, Appl. Phys. Lett. **91**, 083509 (2007).
[3]B. H. Eom, P. Day, H. LeDuc, and J. Zmuidzinas, Nat. Phys. **8**, 623–627 (2012).
[4]J. Y. Qiu, A. Grimsmo, K. Peng, B. Kannan, B. Lienhard, Y. Sung, P. Krantz, V. Bolkhovsky, G. Calusine, D. Kim, A. Melville, B. M. Niedzielski, J. Yoder, M. E. Schwartz, T. P. Orlando, I. Siddiqi, S. Gustavsson, K. P. O'Brien, and W. D. Oliver, Nat. Phys. **19**, 706 (2023).
[5]N. Klimovich, P. Day, S. Shu, B. H. Eom, H. Leduc, and A. Beyer, "Demonstration of a quantum noise limited traveling-wave parametric amplifier," arXiv:2306.11028 [quant-ph] (2023).
[6]M. Malnou, M. Vissers, J. Wheeler, J. Aumentado, J. Hubmayr, J. Ullom, and J. Gao, PRX Quantum **2**, 010302 (2021).
[7]M. R. Vissers, R. P. Erickson, H.-S. Ku, L. Vale, X. Wu, G. C. Hilton, and D. P. Pappas, Appl. Phys. Lett. **108**, 012601 (2016).
[8]C. Bockstiegel, J. Gao, M. Vissers, M. Sandberg, S. Chaudhuri, A. Sanders, L. Vale, K. Irwin, and D. Pappas, J. Low Temp. Phys. **176**, 476 (2014).
[9]S. Chaudhuri, D. Li, K. D. Irwin, C. Bockstiegel, J. Hubmayr, J. N. Ullom, M. R. Vissers, and J. Gao, Appl. Phys. Lett. **110**, 152601 (2017).
[10]W. Shan, Y. Sekimoto, and T. Noguchi, IEEE Trans. Appl. Supercond. **26**, 1801209 (2016).
[11]S. Shu, N. Klimovich, B. H. Eom, A. D. Beyer, R. B. Thakur, H. G. Leduc, and P. K. Day, Phys. Rev. Res. **3**, 023184 (2021).
[12]N. S. Klimovich, "Traveling wave parametric amplifiers and other nonlinear kinetic inductance devices," Ph.D. thesis (California Institute of Technology, 2022).
[13]D. J. Thoen, B. G. C. Bos, E. A. F. Haalebos, T. M. Klapwijk, J. J. A. Baselmans, and A. Endo, IEEE Trans. Appl. Supercond. **27**, 1500505 (2017).
[14]R. Pöpel, IEEE Trans. Magn. **27**, 1306 (1991).
[15]D. C. Mattis and J. Bardeen, Phys. Rev. **111**, 412 (1958).
[16]E. Hammerstad and O. P. Jensen, IEEE MTT-S International Microwave symposium Digest (IEEE, 1980), p. 407.
[17]T. C. Edwards and M. B. Steer, "Appendix A: Transmission line theory," in *Foundations of Interconnect and Microstrip Design* (John Wiley & Sons, Ltd, 2000), pp. 435–447, see https://onlinelibrary.wiley.com/doi/pdf/10.1002/9781118894514.app1.